Statistics of Drop Size Distribution Parameters and Rain Rates for Stratiform and Convective Precipitation during the North Australian Wet Season

Guillaume Penide, Vickal V. Kumar, Alain Protat, Peter T. May

Statistics of Drop Size Distribution Parameters and Rain Rates for Stratiform and Convective Precipitation during the North Australian Wet Season

GUILLAUME PENIDE

Laboratoire d'Optique Atmosphérique, UMR CNRS 8518, Université des Sciences et Technologies de Lille, Villeneuve d'Ascq, France

VICKAL V. KUMAR

Centre for Australian Weather and Climate Research, and School of Mathematical Sciences, Monash University, Melbourne, Victoria, Australia*

ALAIN PROTAT AND PETER T. MAY

Centre for Australian Weather and Climate Research, Melbourne, Victoria, Australia*

(Manuscript received 10 September 2012, in final form 18 February 2013)

ABSTRACT

C-band polarimetric radar measurements spanning two wet seasons are used to study the effects of the large-scale environment on the statistical properties of stratiform and convective rainfall around Darwin, Australia. The rainfall physical properties presented herein are the reflectivity fields, daily rainfall accumulations and raining area, rain rates, and drop size distribution (DSD) parameters (median volume diameter and ''normalized'' intercept parameter). Each of these properties is then analyzed according to five different atmospheric regimes and further separated into stratiform or convective rain categories following a DSD-based approach. The regimes, objectively identified by radiosonde thermodynamic and wind measurements, represent typical wet-season atmospheric conditions: the active monsoon regime, the ''break'' periods, the ''buildup'' regime, the trade wind regime, and a mixture of inactive/break periods. The large-scale context is found to strongly modulate rainfall and cloud microphysical properties. For example, during the active monsoon regime, the daily rain accumulation is higher than in the other regimes, while this regime is associated with the lowest rain rates. Precipitation in this active monsoon regime is found to be widespread and mainly composed of small particles in high concentration compared to the other regimes. Vertical profiles of reflectivity and DSD parameters suggest that warm rain processes are dominant during this regime. In contrast, rainfall properties in the drier regimes (trade wind/buildup regimes) are mostly of continental origin, with rain rates higher than in the moister regimes. In these drier regimes, precipitation is mainly formed of large raindrops in relatively low concentration due to a larger contribution of the ice microphysical processes on the rainfall formation.

1. Introduction

It has been recently shown (Stephens et al. 2010) that the time-integrated accumulations of precipitation produced by global climate models closely match observations when they are globally composited (Stephens et al. 2010). However, this good match is produced by global models through a compensation of errors, with models producing precipitation approximately twice as often as that observed and making rainfall far too light (Stephens et al. 2010). Thus, global models are unable to represent the spatial variability of the precipitation frequency and intensity (Sun et al. 2006). But, if we are to better predict how precipitation patterns might vary in a changing climate, global models must correctly predict both the frequency of occurrence and the instantaneous intensity of rainfall in the present climate.

* A partnership between the Bureau of Meteorology and the Commonwealth Scientific and Industrial Research Organisation.

Corresponding author address: Guillaume Penide, Laboratoire d'Optique Atmosphérique, UMR CNRS 8518, Université Lille1, 59655 Villeneuve d'Ascq CEDEX, France.
E-mail: guillaume.penide@univ-lille1.fr

DOI: 10.1175/MWR-D-12-00262.1

Precipitation patterns and their associated physical processes remain difficult to characterize at different scales because of their large spatial and temporal variability. Thus, long-term observations from active and passive remote sensing instruments such as radars, lidars, and radiometers on the ground or on board satellites represent key datasets that can help improve our understanding of cloud and rainfall properties.

The underlying motivation of this work is to contribute to the improvement of climate models and satellite-based retrievals such as the Tropical Rainfall Measuring Mission (TRMM; Kummerow et al. 1998) and the future Global Precipitation Measurement (GPM) project by providing an observational basis to assess their outputs and, in a second step, to help constrain or build new parameterizations of microphysics for numerical models that would account for the large-scale context [as proposed, for instance, as a new framework for parameterization developments in Jakob (2010)]. The approach considered in the present paper, building on the prior studies of Bringi et al. (2009) and Thurai et al. (2010), uses long time series of observations from the Darwin (Northern Territory, Australia) dual-polarized C-band radar to determine the effect of the large-scale atmospheric environment on the rainfall properties. The underlying question here is: How variable are the rainfall physical properties as a function of the large-scale context? Moreover, this work aims to complement the studies of Protat et al. (2011) on the variability of tropical ice cloud properties (ice water content, visible extinction, effective radius, total concentration) and Kumar et al. (2013) on convective cloud characteristics (life cycle, cloud-top height, electrical activity, cell volume). These studies make use of the same large-scale regime definitions and the same observational periods [as defined in Pope et al. (2009)] in order to build a comprehensive test bed for large-scale model verification of cloud and precipitation properties and also to help improve cloud resolving model (CRM) microphysical parameterizations.

To achieve this, the identification of physically based large-scale regimes is of primary importance, as the synoptic environment inherently drives cloud and rainfall properties at smaller scales. Various large-scale environment definitions could be used for this kind of study (Protat et al. 2011), such as the convective modulation over the tropics defined by the Madden–Julian oscillation (MJO; Madden and Julian 1972) index (Wheeler and Hendon 2004) or the cloud regimes in the tropical western Pacific as defined by Jakob and Tselioudis (2003) within the framework of the International Satellite Cloud Climatology Project (ISCCP; Rossow and Schiffer 1991). But, as the aim of this work is to provide small-scale statistics useful for the evaluation of numerical models and satellite-based retrievals, as well as to inform parameterization development, there is a need to link the rainfall properties to large-scale atmospheric regimes identified with thermodynamical (temperature, dewpoint temperature) and kinematic (horizontal winds) profiles. Indeed, these basic variables, which can be easily measured with radiosondes and simulated in numerical atmospheric models, provide a strong foundation to build and compare long-term statistics.

Statistics of drop size distribution (DSD) parameters and rain rates retrieved from C-band polarimetric radar measurements over Darwin during two consecutive wet seasons (October–April 2005/06 and 2006/07) are analyzed. DSD parameters were retrieved following the technique described in Bringi et al. (2009) and further separated according to five large-scale regimes and two different rain types: stratiform and convective. The dataset used herein is larger than in the previous studies of Bringi et al. (2009) and Thurai et al. (2010), which used only a few days to study the DSD variability as a function of only two regimes (buildup and active monsoon).

2. Methodology

a. C-PoL radar and DSD retrievals

C-Pol (Keenan et al. 1998) is a C-band (5.5 GHz) dual-polarization radar located near Darwin. The C-Pol radar performs a volumetric scan every 10 min within a 150-km scan radius, using 15 elevation angles (from 0.5° to 43.1°) and a range resolution of 300 m. It transmits and receives linear vertical and horizontal polarizations, which give access to key polarimetric variables such as the horizontal reflectivity Z_h, the differential reflectivity Z_{dr}, and the specific differential phase K_{dp}, which are the inputs into the DSD retrieval algorithm of Bringi et al. (2009) that is used in the present study.

In this method, DSD parameters and rain rates are retrieved on each plan position indicator (PPI) scan using a normalized gamma DSD functional form (Testud et al. 2001) described by the median volume diameter D_0 and the ''generalized'' intercept parameter N_w. In this study, N_w is the same as the intercept parameter of an exponential DSD with the same D_0 and liquid water content as the gamma DSD. This algorithm uses a multiparameter approach to take advantage of the complementary information contained in the polarized backscattered signals and has been developed using 6 months of disdrometer data. First, Z_h and Z_{dr} are corrected for attenuation using the ZPHI method [correction of Z_h using the differential propagation phase Φ_{dp} (Testud et al. 2000; Bringi et al. 2001)] and the Tan et al. (1995) approach, respectively. The third input variable, K_{dp}, is

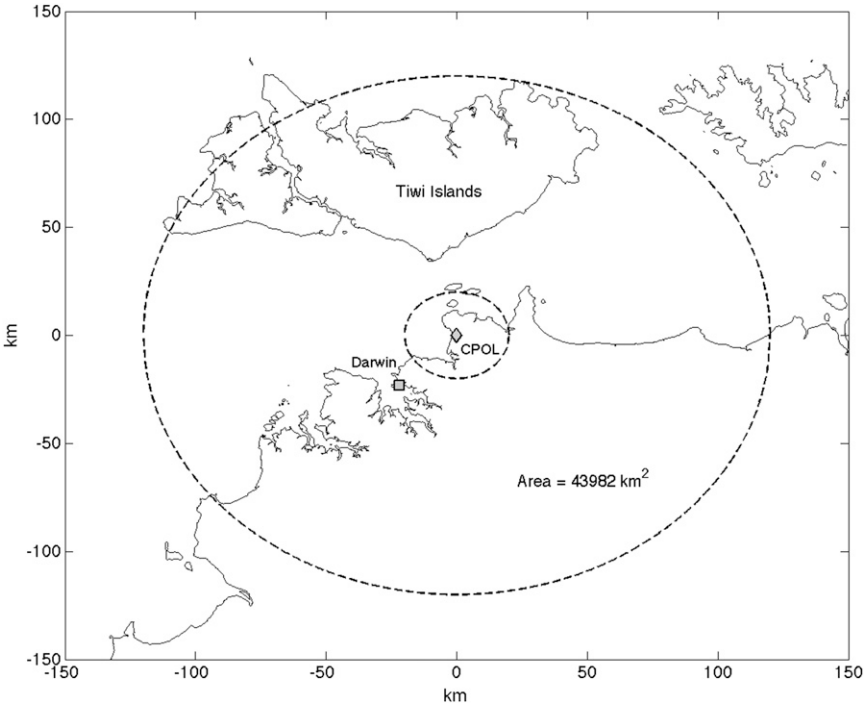

FIG. 1. Location of the C-Pol radar (diamond) near Darwin (square) and of the analyzed area (dashed circles delimitating the [20–120] km around the radar center).

derived from the measured differential propagation phase Φ_{dp} using the finite impulse response (FIR) range filter (Hubbert and Bringi 1995). Note that as a result of large gate-to-gate fluctuations, Z_{dr} was also treated using the FIR range filter. Then, D_0 is retrieved from the differential reflectivity using polynomial fits [i.e., $D_0 = f(Z_{dr})$], N_w is then estimated using a power law from both Z_h and D_0 [$N_w = f(Z_h, D_0)$], and finally the rain rate is estimated using a function of the form $R = f(K_{dp})$, $R = f(Z_h, Z_{dr})$, or $R = f(Z_h)$, depending on various thresholds and a decision tree (Bringi et al. 2009).

Constant-altitude plan position indicators (CAPPIs) at an altitude of 2.5 km are used so that each analysis is realized at the same altitude. This avoids biases from microphysical properties, which vary with height, such as those introduced by the evaporation–coalescence–breakup of raindrops. Each CAPPI is horizontally defined within a radius of 140 km and a horizontal resolution of 2.5 km. To avoid any issues that might appear during the interpolation from PPIs to CAPPIs, only the values in the range 20–120 km are analyzed, which corresponds to a total coverage area of 43 982 km^2, as shown in Fig. 1.

b. Convective–stratiform separation

Many studies have been devoted to the classification of rain types into stratiform and convective parts using rain gauges and/or radar data (Williams et al. 1995; Steiner et al. 1995; Tokay and Short 1996; Biggerstaff and Listemaa 2000; Ulbrich and Atlas 2007; Bringi et al. 2009; Thurai et al. 2010) or visible–infrared–microwave satellite data (Adler and Negri 1988; Anagnostou and Kummerow 1997; Hong et al. 1999). Convective and stratiform parts of cloud systems show significant differences in terms of dynamics and thus in terms of microphysics, so it is obvious that different rain types have to be treated separately in order to extract consistent conclusions.

The approach considered in the present paper was to use a DSD-based separation technique as described in Bringi et al. (2009). They introduced a third class of precipitation, defined as ''mixed'' rain or ''transition'' rain formed from decaying convective cells that have enough microphysical differences from purely stratiform and convective rain types to be considered as a (self-consistent) separate rain class (Williams et al. 1995). They showed that the inherent microphysical differences within the three regimes can be easily identified in the $\log_{10}(N_w) - D_0$ space using a simple linear function (separator criterion) given by

$$\log_{10}(N_w^{sep}) = -1.6D_0 + 6.3, \quad (1)$$

where D_0 is in units of millimeters, N_w is in units of per millimeters per meter cubed, and the superscript sep

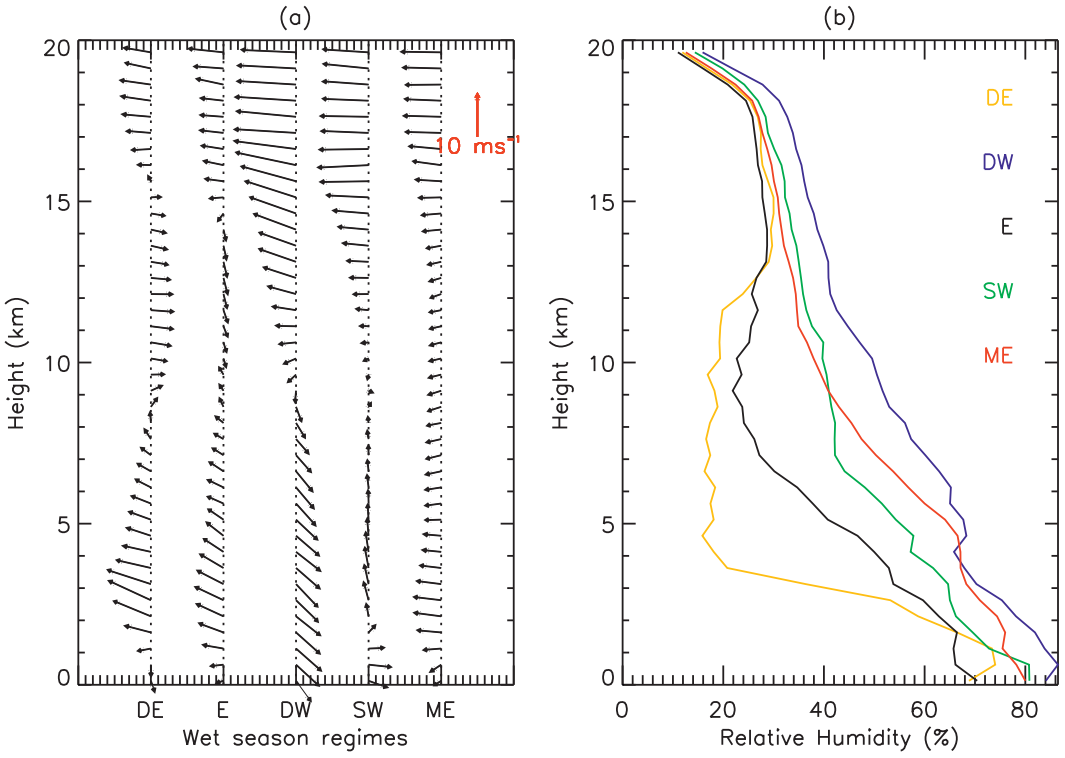

FIG. 2. Two-year mean profiles of radiosonde measurements of (a) horizontal winds and (b) relative humidity, for the five wet-season regimes.

stands for the separator. From this separator criterion, a simple index i defined as the difference between the retrieved $\log_{10}(N_w^{\mathrm{CPOL}})$ and Eq. (1) is calculated:

$$i = \log_{10}(N_w^{\mathrm{CPOL}}) - \log_{10}(N_w^{\mathrm{sep}}). \qquad (2)$$

As a result, large positive values of i refer to convective regions, large negative values of i represent stratiform regions, and low-magnitude values of i, both positive and negative, indicate transition regions.

Bringi et al. (2009) have also compared their classification method with the nonpolarimetric Steiner et al. (1995) approach. Bringi et al. showed by using probability density function (PDF) comparisons of the two techniques that the DSD-based approach allows a more constrained definition of the convective regions without any small values of rain rates, D_0, and N_w (smaller than $10\,\mathrm{mm\,h^{-1}}$, 0.7 mm, and 3.2, respectively). They concluded that this approach seemed more realistic in terms of the definition of convection, and that stratiform regions were as accurately identified as with the texture-based method with the addition of a smoother transition between the two regimes via the introduction of the mixed rain class. As the mixed or "uncertain" category represents only 3% of the dataset, only purely stratiform and purely convective precipitation categories have been used in the following. In addition, two-sample Kolmogorov–Smirnov tests have been realized on every pair of PDFs presented herein in order to test the independency and the statistical significance of the results. The test gives 0 if the two PDFs being tested are totally independent and 1 if the two samples come from the same distribution. We found that the maximum value of all the tests that we realized is about 10^{-6}, which indicates that all the PDFs are clearly independent and that all the comparisons between the PDFs are statistically significant.

c. *Thermodynamic and kinematic large-scale regimes*

Pope et al. (2009) performed a cluster analysis on wind and thermodynamical profiles from daily radiosondes (2300 UTC) launched at Darwin corresponding to 49 wet seasons between 1957/58 and 2005/06. They defined five atmospheric regimes corresponding to different horizontal wind, temperature, and dewpoint temperature profiles. The mean profiles of horizontal wind and relative humidity corresponding to the five atmospheric regimes within our two-wet season dataset are shown in Figs. 2a and 2b, respectively. Additionally, Table 1 summarizes the number of points and the occurrence corresponding to each of the five large-scale regimes, which are then separated into stratiform and convective

TABLE 1. Number of days and occurrences of the five large-scale regimes, and the corresponding stratiform and convective number of points and occurrence used to build the statistics.

Regimes		Dry east	Deep west	East	Shallow west	Moist east
No. of days (%)		37 (10.3)	64 (17.8)	25 (6.9)	59 (16.4)	175 (48.6)
No. of points (%)	Stratiform	149 190 (88.7)	6 183 388 (91.9)	482 655 (89.2)	4 320 299 (92.6)	$1.155\,714\,6 \times 10^7$ (91.4)
	Convective	13 742 (8.1)	342 194 (5.0)	41 151 (7.6)	227 776 (4.8)	705 488 (5.5)

precipitation. The following main features of the five regimes are identified:

- Dry easterly regime (DE)—This regime is characterized by drier than normal southeasterly winds from the surface up to the midtroposphere (7–8 km) and weak northwesterlies above 8 km. As relative humidity decreases dramatically with height compared to the other regimes, the DE regime is considered to be the driest of the five regimes and can be viewed as a trade wind regime. This regime occurs on about 10% of the days in our dataset (Table 1).
- Deep westerly regime (DW)—This regime is composed of northwesterly winds below 7–8 km associated with high humidity and southeasterly winds above 8 km. This regime is identified with the typical active monsoon regime at Darwin (Drosdowsky 1996) and represents about 18% of the days.
- Easterly regime (E)—This regime represents a transition environment (buildup) between the trade winds (DE regime) and the active monsoon (DW regime) (cf. Keenan and Carbone 1992). It has almost the same horizontal wind profile (with lower magnitudes) as the DE regime but is characterized by a moister profile. This regime represents about 7% of the dataset.
- Shallow westerly regime (SW)—This regime is associated with a weaker monsoon circulation than occurs during the DW regime due to an eastward propagation of the MJO (Pope et al. 2009). It is composed of shallow southwesterly winds below 2 km and weak southeasterly winds above with an intermediate moisture profile. This regime can be seen as a mixed inactive and break monsoon regime with a relative occurrence of about 16% during the wet season.
- Moist easterly regime (ME)—This regime is characterized by weak easterlies throughout the entire atmosphere associated with higher humidity profiles than the other easterly regimes. The ME regime corresponds to break monsoon conditions and occurs on about half of the days during the north Australian wet season.

To illustrate the variability and length of each regime, the temporal evolution of the regime classification is shown in Fig. 3. One can see that the active monsoon regime (DW) and the break periods (ME) are the only two regimes that, once established, tend to last several

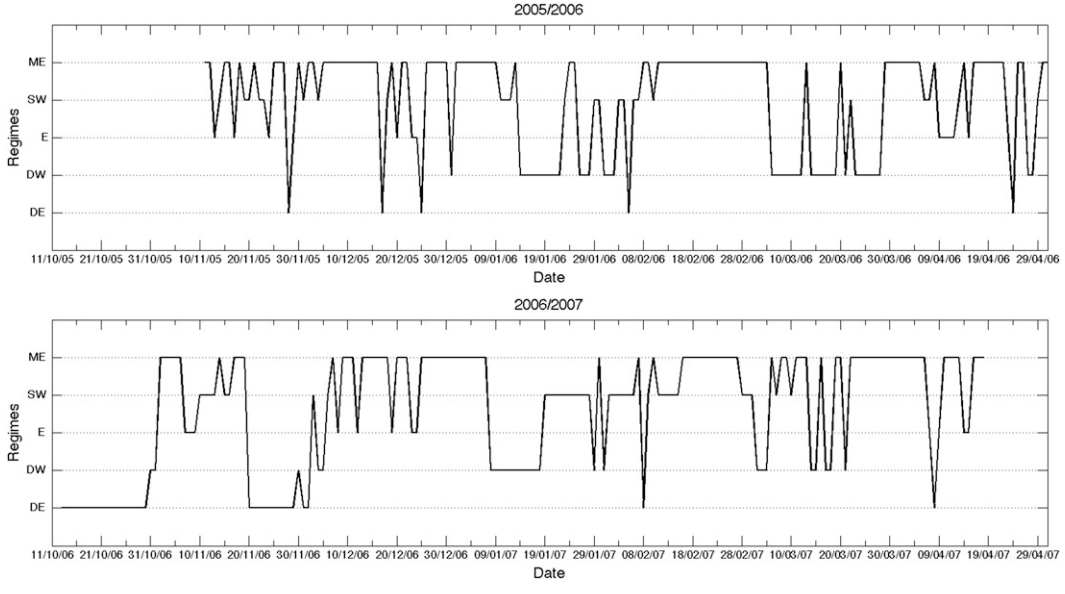

FIG. 3. Temporal evolution of the five large-scale regimes during the two wet seasons (2005/06 and 2006/07).

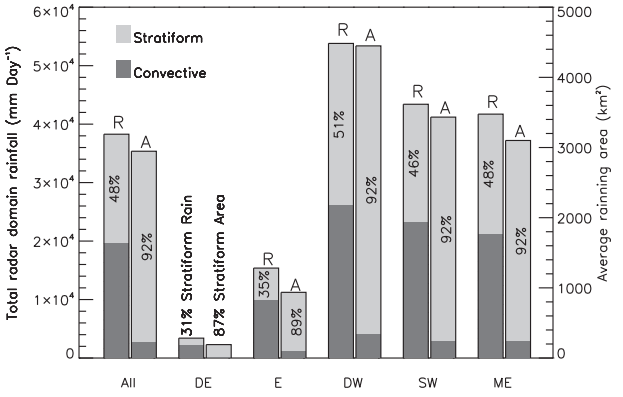

FIG. 4. Bar graph of daily total radar domain rainfall (left bars labeled "R") and average raining area (right bars labeled "A") within 120 km of the radar using all data and separately for the five large-scale atmospheric regimes. Amounts that are convective in nature are shown in a darker shade and the remaining lighter shades represent the stratiform contributions. The stratiform contributions have also been expressed as the percentage of the total.

days. Except during the first two months (October–November) of the 2006/07 wet season, the DE regime is very sparse. The E regime is infrequently represented (only about 7%) and mainly appears between two break periods. Finally, the SW regime has an intermediate pattern of behavior since it tends to last for a few days once established and it almost always appears after the DW regime, which is consistent with the hypothesis that the SW and DW regimes are connected with the eastward propagation of the MJO (Pope et al. 2009).

3. Results

In this section we present an overview of the stratiform and convective rainfall properties as a function of the five Darwin wet season regimes. First, the general patterns of the stratiform and convective precipitation are discussed. Next, the vertical structure of the reflectivity fields and DSD parameters will be analyzed. Finally, the variability of the DSD parameters at 2.5-km height will be presented.

a. Overview of stratiform–convective precipitation during the five Darwin wet-season regimes

Figures 4 and 5 summarize the general patterns of stratiform and convective precipitation corresponding to the five large-scale regimes. Figure 4 shows the daily average rainfall and raining area retrieved from C-Pol measurements, and Fig. 5 illustrates the rainfall spatial variability. It is clear from Fig. 4 that the active monsoon regime (DW) corresponds to the largest precipitation area and the highest daily rainfall accumulation. The DE and E are the driest regimes. The SW and ME regimes are quite similar in terms of rainfall accumulation and raining area with magnitudes closer to the DW regime than to the DE and E regimes. A main difference between the regimes is the convective contribution to the total rainfall, which is only 49% within the DW regime (lowest percentage) while it reaches 65% and 69% within the E and DE regimes, respectively. In addition, the convective contribution to the total raining area varies from 8% (DW, SW, and ME) up to 13% for the DE regime. More stratiform rain is produced during the DW regime as compared to the other regimes (51% versus 48% for ME) due to longer-lived anvil clouds generated by deep convection (May and Ballinger 2007; Protat et al. 2011; Kumar et al. 2013). The active monsoon regime shows a widespread spatial variability over the whole radar scan (Fig. 5) with clear evidence of oceanic and coastal influences (e.g., Keenan and Carbone 1992). The oceanic convection is usually embedded within a clean maritime environment associated with high concentrations of coarse- and fine-mode sulfate aerosols (Allen et al. 2008), while the coastal influence is mainly due to the land- and sea-breeze convergence around Darwin.

Within all the easterly regimes, large daily rainfall accumulations are located on the western part of the Tiwi Islands, off the coast of northern Australia (Fig. 5). This particular feature of the easterly regimes can be attributed to the strong interactions between sea breezes and cold pools that often evolve in mesoscale convective systems (MCSs; a.k.a. Hectors) when gust fronts amplify the convection along the zonal breeze fronts (Carbone et al. 2000). During the dry easterly regime, convective precipitation is mainly present over the Tiwi Islands with only a weak coastal influence while the E regime exhibits a much more widespread area of coverage with a noticeable coastal influence. The ME regime also exhibits secondary maxima over the inland sector and over the Australian western coast. Finally, precipitation within the SW regime has no real preferential geographical location (Fig. 5). During this regime, the accumulated rainfall and the convective contribution to rainfall are slightly larger than average (54% versus 52%; Fig. 4).

b. Vertical structure of stratiform–convective precipitation during the five Darwin wet-season regimes

To further analyze the regime dependence of rainfall parameters in terms of microphysical processes, vertical information is needed. Figure 6 shows the height-dependent probability density functions of reflectivities [hereafter HPDF, as defined in Protat et al. (2010)], and Fig. 7 shows the mean profiles of D_0 and N_w together with, at each CAPPI level, a bar representing the "interquartile range" (i.e., the range within which 50% of

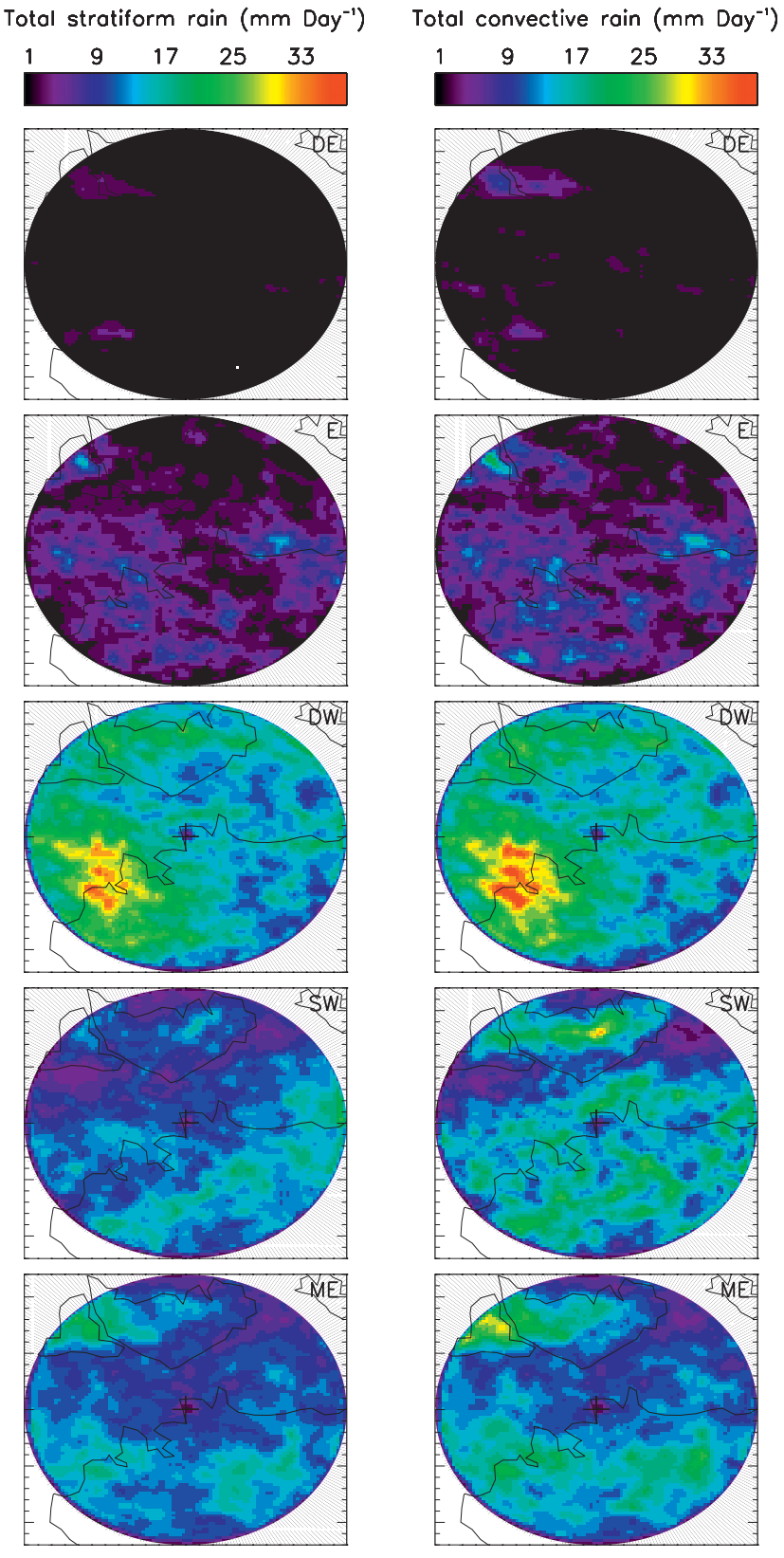

FIG. 5. Daily rainfall accumulations during the five different large-scale atmospheric regimes and separately for (left) stratiform and (right) convective precipitation. The total area is shown in pixels of 2.5 km × 2.5 km.

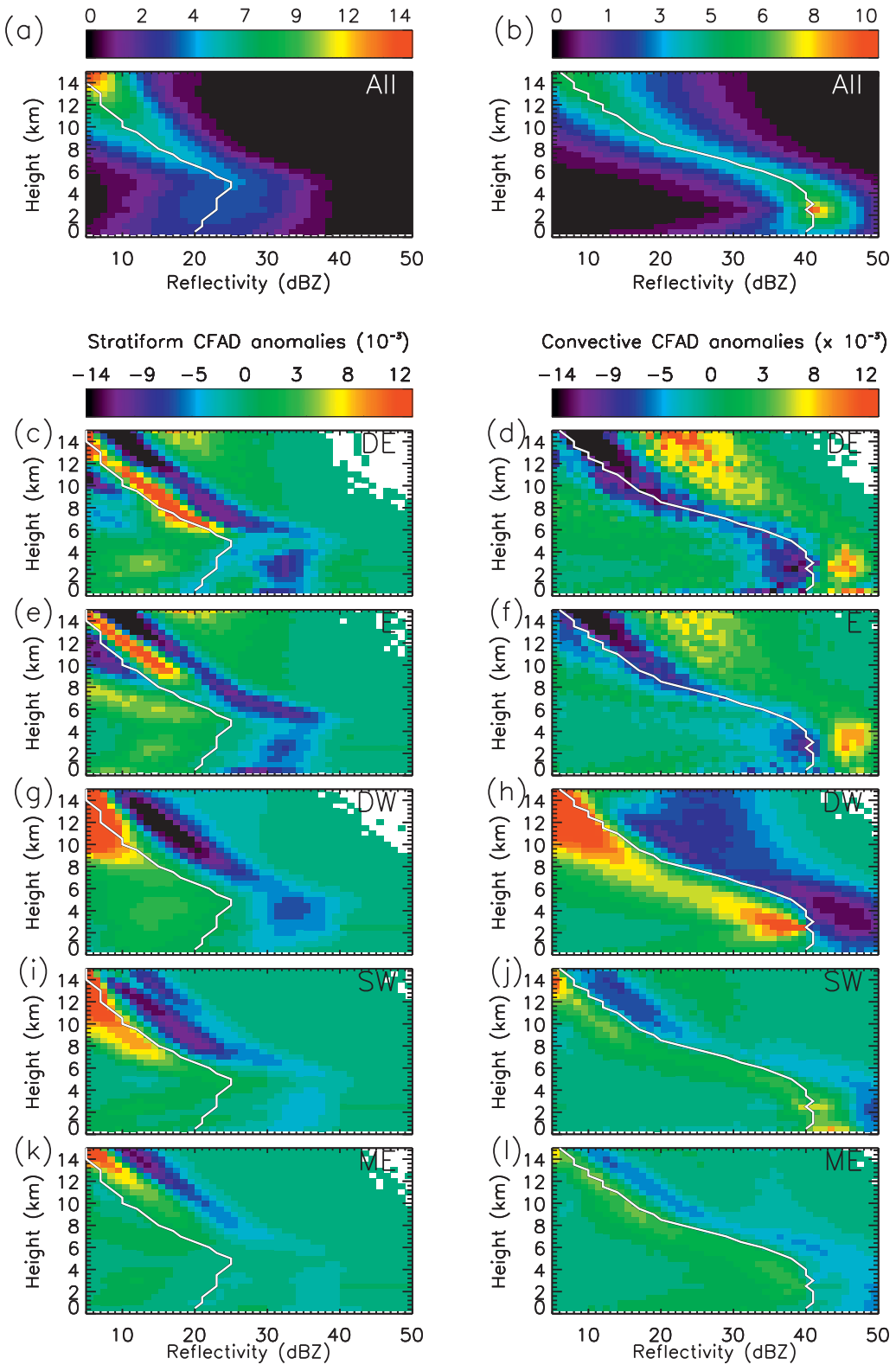

FIG. 6. HPDFs of (a) stratiform reflectivity and (b) convective reflectivity (% $\mathrm{dB}Z^{-1}\,\mathrm{km}^{-1}$); together with the HPDFs of reflectivity anomalies within the five regimes (e.g., regime total, 10^{-1}% $\mathrm{dB}Z^{-1}\,\mathrm{km}^{-1}$). (left) The stratiform precipitation and (right) convective rainfall. (top) White lines in the HPDFs of reflectivity anomalies represent the mode values corresponding to the total HPDFs. From top to bottom, regimes are organized as follow: DE, E, DW, SW, and ME.

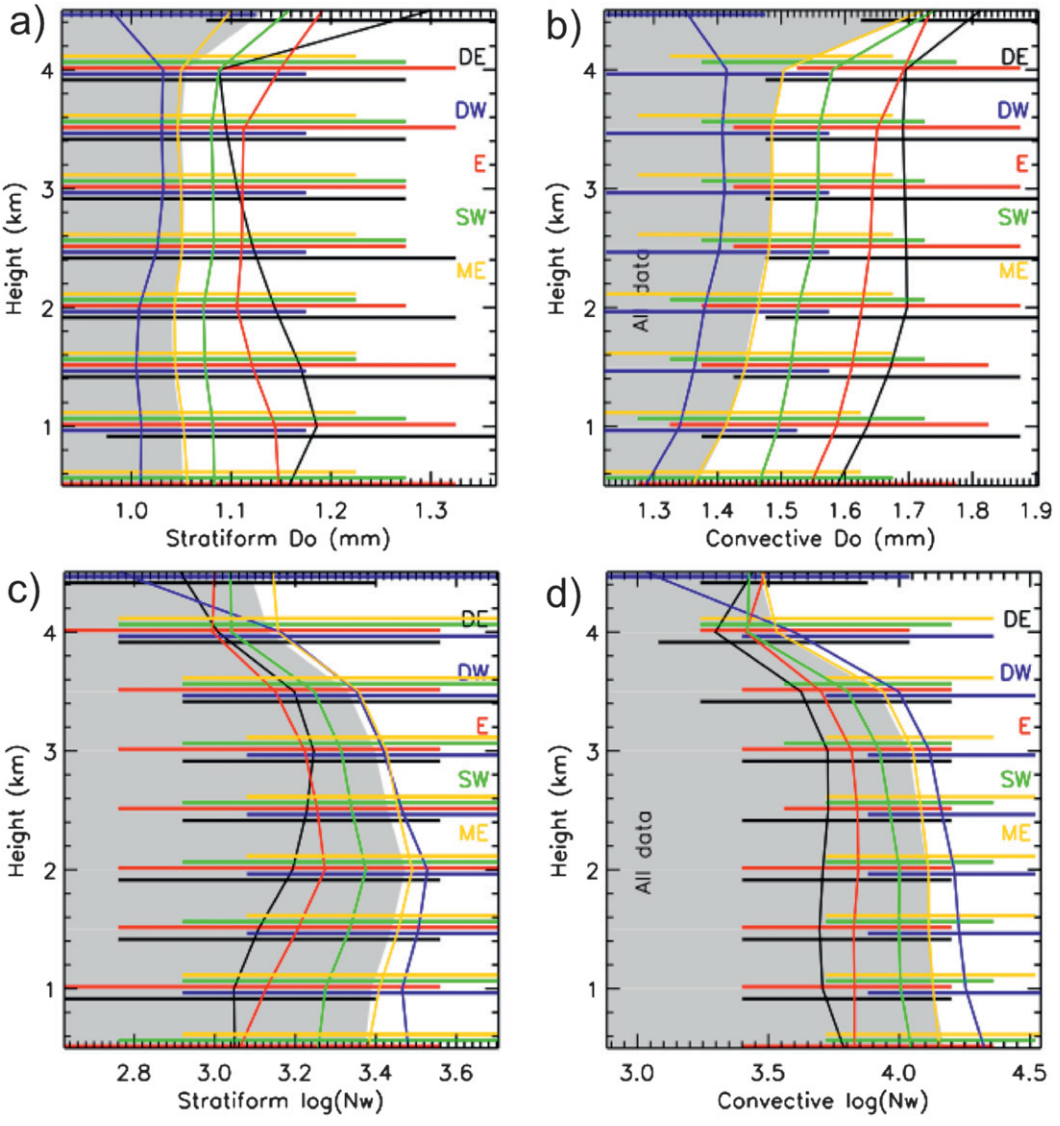

FIG. 7. Mean vertical profiles of (a),(b) D_0 and (c),(d) $\log_{10}(N_w)$ for the five large-scale regimes and separated into (a),(c) stratiform and (b),(d) convective precipitation. The shaded area represents the whole dataset. At each CAPPI level (i.e., every 500 m), bars representing the interquartile range for each regime are also represented. The interquartile range represents the difference between the third and the first quartiles (i.e., the range within which are located 50% of the population around the median value).

the population around the median value is located). Two kinds of HPDFs are presented in Fig. 6; the top two HPDFs are built considering all the stratiform and convective points (Figs. 6a and 6b, respectively), and the remaining panels represent the HPDFs of reflectivity anomalies (i.e., regime − total) corresponding to the five regimes and separated in stratiform (left-hand side in Fig. 6) and convective precipitation (right-hand side). Figures 6a and 6b exhibit very common features relative to the stratiform and convective precipitation (Yuter and Houze 1995). The HPDF of stratiform precipitation (Fig. 6a) shows a slow increase in the reflectivities with decreasing height from 14 to 5 km (the approximate altitude of the 0°C isotherm), followed by a slight decrease in liquid phase toward the surface. The increase in the reflectivities from 14 to 5 km can be explained by the growth processes of ice particles, such as the aggregation and diffusional growth processes, which are preponderant in stratiform clouds (e.g., Houghton 1968; Yuter and Houze 1995; Houze 1997; McFarquhar et al. 2007; Penide et al. 2010; Protat et al. 2011). The decreasing reflectivities from the melting level toward the surface can

be interpreted as a combination of the evaporation and breakup processes, which tend to decrease the particle diameters and thus the reflectivities. Moreover, Figs. 7a and 7c clearly show that, when considering all the data (shaded area), there is a quasi-constant D_0 value from 4 to 2 km associated with increasing values of N_w, which can be interpreted as a competition between coalescence and breakup leading to an increase in the number of both small and large particles that could explain the constant median volume diameter (hydrometeors such as aggregates, once melted, can lead to large and unstable drops). In addition, the slight increase in LWC (not shown) from 4 to 2 km can be explained by the growth of the particles in a humid environment. Indeed, at such altitudes additional condensational growth and/or accretion of cloud water may contribute to the increase in mass. These processes are sensitive to the local dynamics and thermodynamics as well as to the DSD shape, given that small droplets evaporate first and that breakup is mainly related to the larger raindrops.

In contrast, the HPDF of the convective precipitation (Fig. 6b) exhibits a different pattern of vertical behavior. There is a steeper increase in the reflectivity mode from 14 km down to 4-km altitude (compared to the stratiform HPDF; Fig. 6a), followed by a quasi-constant mode of reflectivity toward the surface (around 42 dBZ). The faster increase of the convective reflectivity mode with decreasing height is due to the difference between the growth processes involved. Convective clouds have larger updrafts than do stratiform clouds, resulting in different ice crystal microphysics notably via the activation of the riming process. Usually, large rimed hydrometeors such as hail or graupel are created exclusively within the convective parts of tropical thunderstorms and mainly above the melting layer where there is supercooled water available (e.g., Ludlam 1950; Houghton 1968; Musil 1970; Browning et al. 1976; Houze 2004). Reflectivities associated with these types of hydrometeors increase rapidly with decreasing height, which explains the different slope found between the stratiform and convective regions at these levels. Once created, these large and dense hydrometeors fall rapidly and thus take time to melt after they fall through the 0°C isotherm so that they are not associated with a well-defined melting layer (bright band). Thus, the reflectivity maximum is observed between 2 and 4 km (i.e., below the 0°C level) due to the presence of both melting hail (and/or graupel) and large raindrops (coming from melted ice crystals) that are not as affected by the evaporation process as stratiform precipitation, but where the collisional processes (breakup and coalescence) dominate (Hu and Srivastava 1995). The increase of the HPDF width close to the ground is due to the cumulative effect of both large raindrops' breakup and coalescence processes, which have opposite consequences on the DSD parameters (i.e., the coalescence process increases D_0 and decreases N_w, whereas breakup decreases D_0 and increases N_w). Therefore, a wide range of possible reflectivity values can be observed according to the different relative efficiencies of these two processes within the 2-yr dataset. Nevertheless, the vertical profiles of convective D_0 and N_w (Figs. 7b and 7d) show that, within all the regimes, there is a slow decrease of D_0 from 4 to 3 km associated with a large increase in N_w, which is the signature of the breakup process. But, as D_0 decreases faster between 2 km and the surface, the breakup process between 3 and 4 km must be in competition with the coalescence process that has the opposite effect on the DSD parameters, as explained previously. Then, from 3 km to the surface there is a steeper decrease of D_0 associated with a slightly increasing N_w for DW, ME, and SW, while it is almost constant for DE and E. This may be interpreted as being a competition between an enhanced breakup process (and/or the activation of the evaporation process in addition to the breakup one, but this is less probable in convective precipitation) that is compensated, at least in terms of N_w, by the coalescence process (and/or, to a lesser extent, by the evaporation process).

The HPDFs of reflectivity anomalies show that there are some fundamental differences between the five regimes. For example, during the DE and E regimes, convection is rare but very intense (Figs. 6d and 6f) and corresponds to larger than average reflectivities in the lower levels (between 40 and 50 dBZ). These large reflectivity values are correlated with the larger relative occurrence of high-level ice clouds with reflectivities in the 20–40-dBZ range that are mainly generated by deep convection (Protat et al. 2011; Kumar et al. 2013). These large reflectivities in the DE and E regimes are also associated with the largest mean median volume diameters (Fig. 7b) and with the largest rain rates (see the tails of the black and red PDFs of rain rates in Fig. 8b), with averages of 33.4 and 32.1 mm h^{-1}, respectively. These two regimes also generate very different signatures in the stratiform part (compared to the other regimes) in response to different convective parts. This includes a much wider distribution of the reflectivities (Figs. 6c and 6e) in the ice-only region (positive anomalies on both sides of a negative anomaly indicate a broader distribution at these levels) as well as additional structures with, notably, a strong bimodality (two maxima at a given altitude) above 8 km that is not present within the other regimes. These large differences, compared to the other regimes, can be explained by the larger variability of the convective cell intensities within

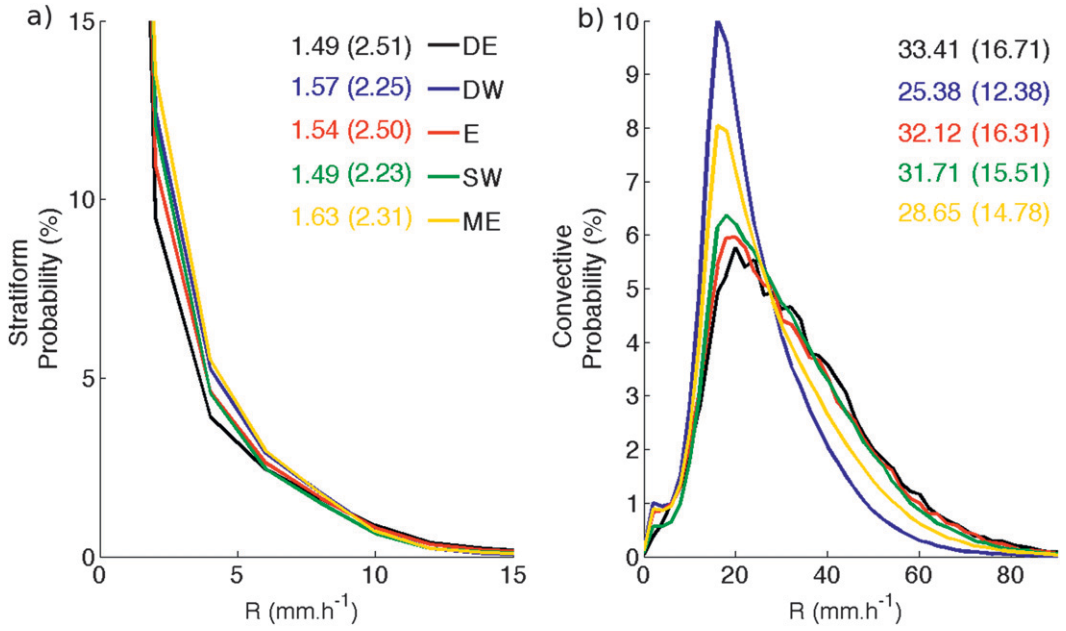

FIG. 8. PDFs of (a) stratiform and (b) convective rain rates separated according to the five large-scale regimes. Means and standard deviations (in brackets) for each PDF are also represented. Bins of 1 mm h^{-1} have been used.

the E and DE regimes (Kumar et al. 2013), yielding a wider range of stratiform cloud properties. Nevertheless, an important part of the distributions in the upper levels (above 8 km) is associated with large reflectivities, so ice particles are larger than in the other regimes, yielding a weaker vertical reflectivity gradient (variation of the reflectivity toward the 0°C level). At lower levels (i.e., below the 0°C level), one can see clear signatures of large positive anomalies that rapidly decrease toward the ground. This is the result of a more efficient evaporation process due to the drier environment in the E and DE regimes. Indeed, Fig. 7a shows that the E and DE regimes are the only two regimes that exhibit an increase in D_0 from 2 km toward the surface associated with a decrease in N_w (Fig. 7c), which is the signature of the evaporation process at those levels (Li and Srivastava 2001; Kumjian and Ryzhkov 2010). Moreover, the positive anomaly mode within the DE regime (Fig. 6c) is slightly shifted toward smaller reflectivity values compared to the E regime (Fig. 6e), which indicates an even more important role of the evaporation within the DE regime that is also clearly visible in the vertical profiles (Fig. 7) as D_0 increases not only from 2 km toward the ground but from 4 km in altitude to the ground.

Convective precipitation within the DW regime (active monsoon; Fig. 6h) is characterized by a large shift (5–10 dBZ) of the main reflectivity mode toward smaller values through the whole troposphere (similar to the stratiform precipitation) with a larger occurrence of low-reflectivity/high-level clouds compared to the climatology. This feature demonstrates that during the active monsoon regime, convection is less intense. Indeed, 25% of the DW convective points have reflectivities below 40 dBZ (at 2.5 km), which is a higher fraction than in the other regimes: DE = 8%, E = 13%, SW = 14%, and ME = 20%. Moreover, the vertical profile of the mean D_0 (Fig. 7b) shows smaller magnitudes within the DW regime compared to the others from the 0°C level toward the surface. These results may be explained by the presence of more cells embedded within large areas of stratiform clouds typical of monsoon conditions. Some of these cells may be in their mature/decaying phase, but considering the large dataset used herein it seems more probable that these cells are overall associated with weaker updrafts (May and Ballinger 2007). Moreover, this is consistent with the vertical reflectivity gradient in the DW regime, which is larger than in the other regimes, especially between 4 and 10 km in altitude. This implies that ice microphysical processes (mainly aggregation and riming) play a less important role in the convective precipitation pattern, as it tends to act on a smaller depth (only between 4 and 8 km roughly) compared to the E and DE regimes. Thus, convective rain rates within this regime are naturally smaller than in the other regimes (Fig. 8b) with a mean value of 25.3 mm h^{-1} (compared to 33.4 mm h^{-1} within the DE regime).

During the SW regime, convective parts are characterized by larger reflectivities than average in liquid phase (from the HPDF anomaly; Fig. 6j) that correspond

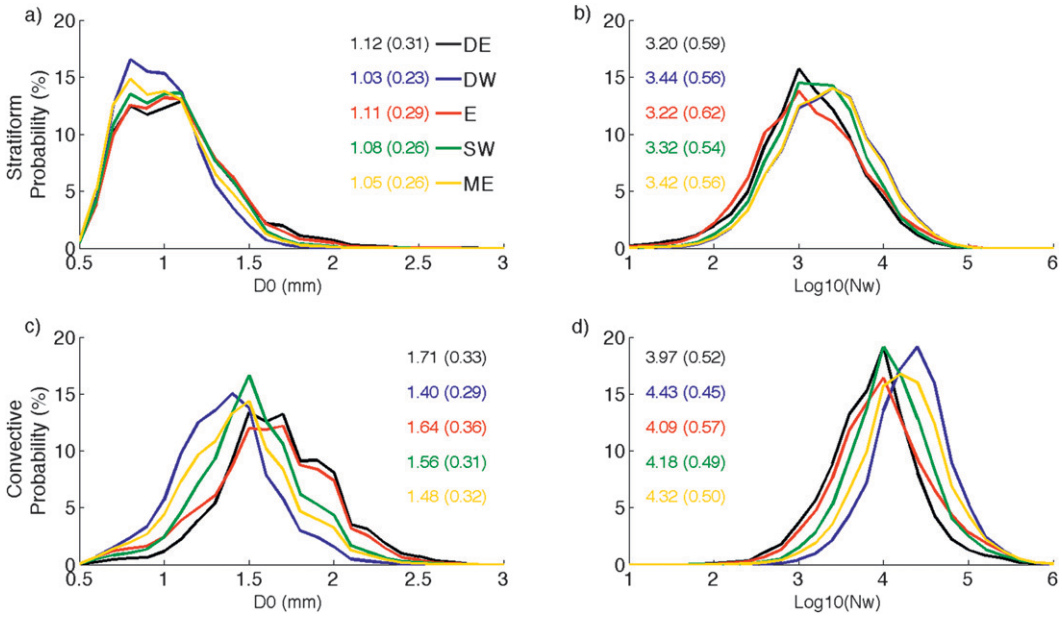

FIG. 9. PDFs of the DSD parameters: D_0 and $\log_{10}(N_w)$ for the five large-scale regimes and separated according to the precipitation type. The (a),(b) stratiform precipitation and (c),(d) convective rainfall. Means and standard deviations (in brackets) for each PDF are also represented. Bins of 0.1 mm (D_0) and 0.2 [$\log_{10}(N_w)$] have been used.

to larger raindrops (Fig. 7b). This is consistent with the fast increase in the reflectivity mode with decreasing height in the ice phase, which indicates the presence of large ice crystals as explained earlier. As shown in Kumar et al. (2013), the SW regime is the most efficient regime at producing deep convective, electrically active, and long lasting (MCS like) storms. Both statistics for the 5-dBZ cloud-top heights and the electrical activity are clearly highest in the SW regime, followed by the easterly regimes (DE/E and ME) and, finally, the DW regime. These convective parts are associated with increased frequencies of occurrence of large rainfall (mean value of 31.7 mm h^{-1}; Fig. 8b). Interestingly, these larger frequencies of occurrence of liquid phase reflectivities are associated with a wider distribution of ice-phase reflectivities (i.e., a larger difference between the two extrema of positive anomalies). But, compared to the other regimes that exhibit the same bimodality in the distribution of the convective reflectivity anomalies (i.e., E and DE), this variability is not translated in the resulting stratiform ice parts of the storms during the SW regime (no more bimodality). This might indicate that the transfer of ice particles from the SW convective part to the stratiform part is different than in the other regimes. Presumably, as the mode associated with the large reflectivities has disappeared, smaller ice particles are transferred and/or generated in the SW stratiform part.

Finally, the ME regime (break) shows a clear and simple signature both in the convective and stratiform parts (Figs. 6k and 6l). The vertical reflectivity gradient is quite similar to that of the DW regime but associated with larger reflectivities, which correspond to bigger hydrometeors than in the DW regime (Fig. 7b). This is consistent with the fact that ME and DW are the two regimes that generate most of the total precipitation and exhibit identical convective–stratiform contributions to the raining area (Fig. 4), but with more rain produced by the convective part in the ME regime (52% versus 49%). Thus, the convective rain rate is slightly larger than in the DW regime with a mean value of 28.6 mm h^{-1} (Fig. 8b).

c. *PDFs of DSD parameters for the five large-scale regimes*

As shown in the previous section, each large-scale regime is associated with different predominant cell types: deep–shallow convection, stratiform–convective rainfall contribution, life cycle, geographical location, and all of these features are dependent on both the thermodynamical environment and the vertical velocity field (May and Ballinger 2007). Moreover, as these thermodynamic and vertical velocity fields drive the cloud microphysics, it is worthwhile to analyze the statistical differences that may exist on the DSD parameters.

PDFs of DSD parameters [D_0 and $\log_{10}(N_w)$] for the five wet-season regimes and separated according to the rain type are presented in Fig. 9. The first noteworthy result is that whatever the parameter and precipitation

type considered, the width (standard deviation, marked in Fig. 9) of the PDF is smaller during the DW regime (active monsoon), where ice microphysical processes are expected to have a smaller impact on precipitation. The main differences between the regimes appear when comparing the ''moist'' regimes (DW and ME) with the ''dry'' ones (DE and E); the shallow westerly regime exhibits an intermediate pattern of behavior. This observation is well marked in the convective PDFs (Figs. 9c and 9d) while it is less obvious in the stratiform ones (Figs. 9a and 9b).

Even though the differences are small in Figs. 9a and 9b, a noticeable fraction of the stratiform precipitation during the E and DE regimes (considering the number of points used to build the PDFs; Table 1) have higher values of D_0 (above 1.2 mm) and lower values of $\log_{10}(N_w)$ (below 3.5; e.g., 3160 mm^{-1} m^{-3}) compared to the other regimes. These differences might be attributed to the larger influence of ice processes on the production of rainfall (Thurai et al. 2010) in addition to the evaporation of the smallest droplets during their fall, which tends to decrease the number of small hydrometeors, thereby increasing the median volume diameter. Contrary to the dry regimes, higher concentrations of small raindrops are observed during the active monsoon (DW) and break periods (ME), both in stratiform and convective precipitation, which strengthens (from a statistical point of view) the results of previous studies (May and Ballinger 2007; Bringi et al. 2009; Thurai et al. 2010; May et al. 2011; Munchak et al. 2012).

Differences among regimes in the ''convective'' PDFs are larger, indicating that the large-scale environment clearly affects the DSD characteristics. Mean median volume diameters for convective rain vary from 1.40 mm during the DW regime to 1.71 mm during the DE regime, which corresponds to a variation of about 18% in terms of mean D_0 while there is a factor of 2.8 between the means of the corresponding N_w. Even though the behavior of D_0 and N_w is generally opposite (as shown in Figs. 7c and 7d), it is interesting to combine those two variables to explore the variation of the associated LWC. Figure 10 represents the PDF of the LWC calculated following Testud et al. (2001) and assuming a constant shape parameter of $\mu = 1$. It is interesting to note in Fig. 10 that, whatever the regime considered, the LWC of the convective rainfall is very similar due to the compensation between the size and the concentration. However, the mean LWC corresponding to the active monsoon and the break regime are slightly greater than for the DE and E regimes, which can be explained by the fact that LWC is mainly carried by the smaller hydrometeors and that both ice processes and evaporation play a key role within the E and DE regimes. This also

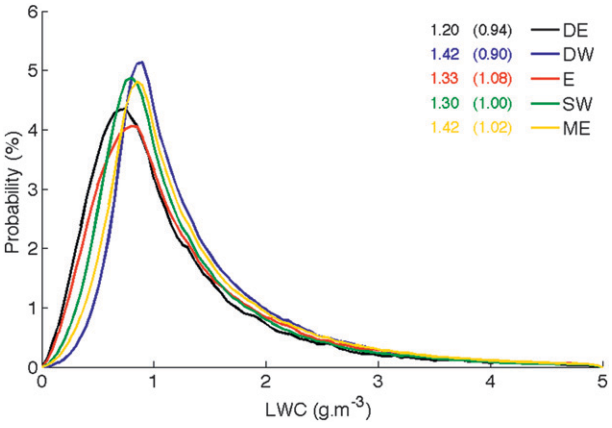

FIG. 10. PDFs of LWC ($g\,m^{-3}$) calculated following Testud et al. (2001) and assuming a shape parameter $\mu = 1$ for the convective precipitation within the five large-scale regimes together with the means and standard deviations (in brackets). Bins of 0.05 $g\,m^{-3}$ have been used.

explains the differences in term of skewness in the distributions. The DE and E regimes have a small positive skewness (0.11, and 0.07, respectively) whereas DW, SW, and ME have a well-marked positive skewness (0.34, 0.23, and 0.29, respectively), which represents the signature of the larger amount of small droplets. May et al. (2011) investigated the impact of aerosols on DSD parameters and noticed that high positive values of skewness in the N_w distributions were correlated to enhanced aerosol loadings. They also showed that in low aerosol concentration regimes larger supercooled droplets are advected within the convective towers, which is consistent with the presence of larger ice crystals and raindrops within the E and DE regimes.

To further investigate these differences and make sure they are not simply as a result of differences in reflectivity PDFs among regimes, conditional PDFs were also built in reflectivity bins. Figure 11 shows conditional PDFs of rain rates and DSD parameters relative to convective precipitation and separated according to both large-scale regimes and reflectivity ranges (bins of 5 dBZ were used). First, one can see that below 40 dBZ, PDFs of rain rates are very similar within the five regimes with only a few differences in terms of relative occurrence. PDFs of DSD parameters show more differences and notably a clear secondary mode within the DE and E regimes, where the other regimes exhibit a slightly decreasing (D_0) or increasing (N_w) slope of the PDF. Size sorting within developing cells and/or evaporation (which can be efficient since $Z_h < 40$ dBZ) could be good candidates to explain this secondary mode, as these processes produce an increase in D_0 and a decrease in N_w (Li and Srivastava 2001; Kumjian and Ryzhkov 2012). This secondary peak in the DE and E regimes could also

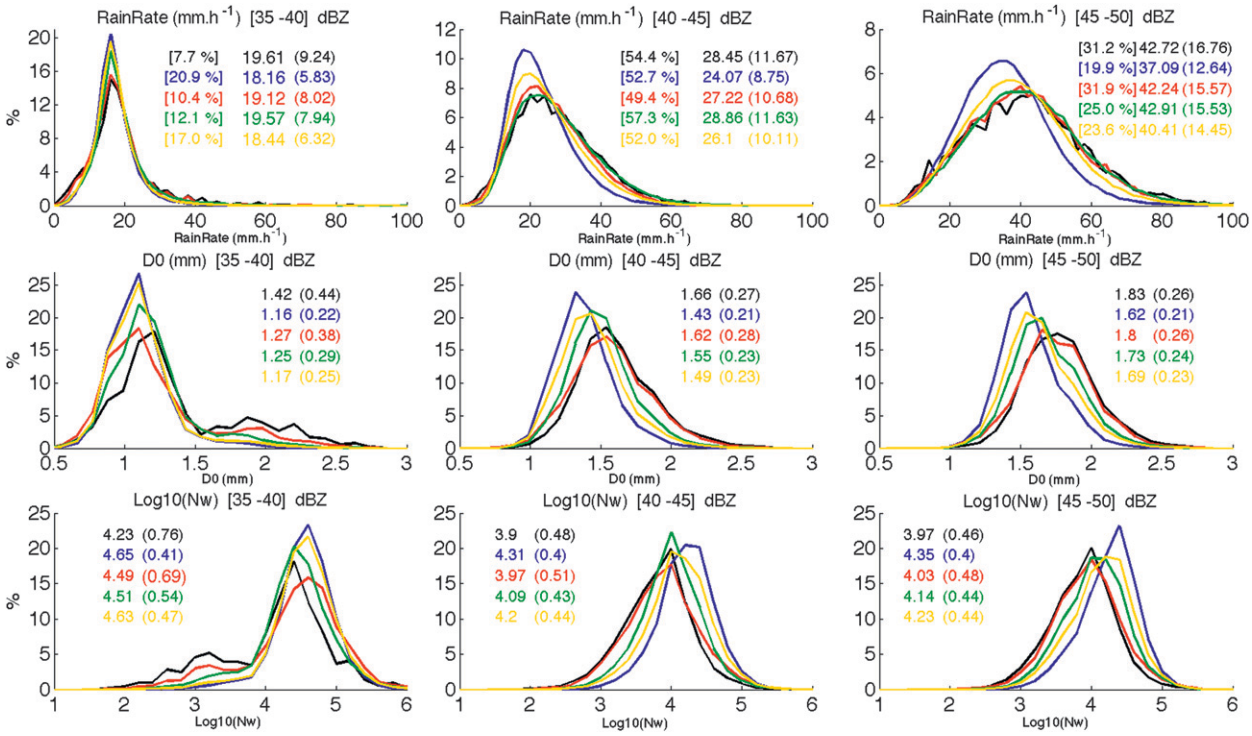

FIG. 11. Conditional PDFs of (top) rain rates, (middle) D_0, and (bottom) $\log_{10}(N_w)$ for convective precipitation according to various reflectivity ranges (5-dBZ bins between 35 and 50 dBZ) and separated according to the five large-scale regimes. Means and standard deviations (in brackets) also appear in each panel. Note that, in the first row, the relative occurrences of the number of points used, within each regime, to build the corresponding PDFs are also represented in square brackets.

be due to the lack of representativeness in these regimes. For example, less than 8% of the DE convective points were used to build the PDF in the 35–40-dBZ range compared to almost 21% of the DW convective points, and the second peak represents 27% of these points (i.e., a total of about 280 points scattered within the 2-yr scans). The main statistical differences appear in the 40–45- and 45–50-dBZ ranges because they represent together about 75%–80% of all the convective points. One can see that PDFs of rain rates are very different between the 40–45- and 45–50-dBZ ranges, as means and the standard deviations increase by about 50% whereas there is only a slight shift (same shape) in the corresponding PDFs of D_0 and N_w toward larger values without any increase in the standard deviations. Indeed, a small increase in the mean diameter of 10% leads to an increase of about 30% in terms of the mean raindrop volume, which, associated with a 17% increase in the number concentration, explain, in part, the 50% variation of the rain rate.

4. Conclusions

In this paper, a 2-yr dataset collected using a C-band dual-polarization radar (C-Pol) located near Darwin, Australia, is used to extract statistics of stratiform and convective precipitation within five large-scale regimes. The statistical properties presented in the present paper are the total daily rainfall accumulations and raining area, the spatial variability of the daily rainfall accumulations, the vertical variability of the reflectivity fields and DSD parameters retrieved following Bringi et al. (2009), and the probability density functions of rain rates and DSD parameters at a constant altitude of 2.5 km. Each of these properties is then examined as a function of five large-scale atmospheric regimes and separately for stratiform and convective rainfall.

The main results can be summarized as follows:

- First, as this paper is based on preliminary studies by Bringi et al. (2009) and Thurai et al. (2010) but using a much larger dataset and a different approach concerning the definition of the regimes, their main conclusions on the active monsoon regime (DW) and the buildup one (DE) needed to be checked/strengthened (from a statistical point of view) and extended using vertical variability analysis.
- Precipitation is mostly of convective origin within the DE and E regimes while the convective–stratiform precipitation ratio is around unity for the other regimes. SW and ME have almost the same total rainfall

accumulation and average raining area. The DW regime produces the most daily precipitation. However, since the ME regime occurrence composes 50% of the wet season, it is the main contributor to the annual rainfall in this region.

- Spatial maps of total rainfall accumulation show that stratiform rainfall and convective rainfall are strongly correlated in space. All of the ''easterly'' regimes (DE, E, and ME) have a maximum over the Tiwi Islands and have a noticeable coastal influence. ''Westerly'' regimes show a more scattered precipitation pattern over the whole domain. The DW regime has a strong coastal influence, mainly over the western part of the radar domain, whereas during the SW regime precipitation is widespread with a weak land influence.
- The differences in terms of vertical reflectivity gradient and DSD parameter profiles highlight clear differences between the regimes such as the larger impact of the evaporation process during the E and DE regimes, or the fact that the active monsoon regime is predominantly associated with warm rain processes whereas the other regimes are more sensitive to ice microphysical processes.
- PDFs of stratiform rain rates show a nearly identical pattern of behavior whatever the regime considered. PDFs of convective precipitation show that all the regimes have a peak of occurrence at $18\,\mathrm{mm\,h^{-1}}$ and then differ according to the shape of the decreasing slopes. The moist regimes (DW and ME) are associated with the lowest convective rain rates and standard deviations compared to the dry regimes (DE and E).
- PDFs of DSD parameters exhibit significant differences according to the environmental conditions. The active monsoon regime (DW) exhibits the narrower distributions of both D_0 and N_w for both rain types. The DW regime has the highest concentrations of small droplets, followed by the ME (break), the SW, and finally the driest regimes (E and DE). Conditional PDFs have also shown that the shape of the PDF of the DSD parameters was very similar between the 40–45- and 45–50-dBZ ranges, which represent more than 75% of the convective points.

Based on the present study and the previous ones of Protat et al. (2011) and Kumar et al. (2013), it is clear that cloud and precipitation statistical properties are strongly linked to the environmental conditions (i.e., large-scale forcing). Such complementary results on ice cloud (Protat et al. 2011) and convective cell properties (Kumar et al. 2013), as well as on precipitation characteristics (this paper), provide a comprehensive picture of the statistical properties of cloud systems as a whole in this area. Moreover, they offer a nearly complete observational basis to assess model parameterizations and satellite retrievals in light of this regime framework. Further developments in model parameterizations and retrieval algorithms can also be guided by comparing the statistics as a function of large-scale atmospheric regimes. As a future work, and with the aim of having an even more complete (and unprecedented) picture of the statistical properties of the tropical troposphere in this region, aerosol physical and chemical properties should also be studied as a function of the same large-scale atmospheric regimes.

Acknowledgments. Part of this work has been supported by the U.S. Department of Energy Atmospheric Radiation Measurement Program. The authors would like to acknowledge the contributions of Brad Atkinson, Dennis Klau, and Michael Whimpey in supporting the Darwin CPOL radar operations and data management, as well as Susan Rennie, Justin Peter, and the three anonymous reviewers for providing helpful comments on the manuscript.

REFERENCES

Adler, R. F., and A. J. Negri, 1988: A satellite infrared technique to estimate tropical convective and stratiform rainfall. *J. Appl. Meteor.,* **27,** 30–51.

Allen, G., and Coauthors, 2008: Aerosol and trace-gas measurements in the Darwin area during the wet season. *J. Geophys. Res.,* **113,** D06306, doi:10.1029/2007JD008706.

Anagnostou, E. N., and C. D. Kummerov, 1997: Stratiform and convective classification of rainfall using SSM/I 85-GHz brightness temperature observations. *J. Atmos. Oceanic Technol.,* **14,** 570–575.

Biggerstaff, M. I., and S. A. Listemaa, 2000: An improved scheme for convective/stratiform echo classification using radar reflectivity. *J. Appl. Meteor.,* **39,** 2129–2149.

Bringi, V. N., T. D. Keenan, and V. Chandrasekar, 2001: Correcting C-band radar reflectivity and differential reflectivity data for rain attenuation: A self-consistent method with constraints. *IEEE Trans. Geosci. Remote Sens.,* **39,** 1906–1915.

——, C. R. Williams, M. Thurai, and P. T. May, 2009: Using dual-polarized radar and dual-frequency profiler for DSD characterization: A case study from Darwin, Australia. *J. Atmos. Oceanic Technol.,* **26,** 2107–2122.

Browning, K. A., and Coauthors, 1976: Structure of an evolving hailstorm. Part V: Synthesis and implications for hail growth and hail suppression. *Mon. Wea. Rev.,* **104,** 603–610.

Carbone, R. E., J. W. Wilson, T. D. Keenan, and J. M. Hacker, 2000: Tropical island convection in the absence of significant topography. Part I: Life cycle of diurnally forced convection. *Mon. Wea. Rev.,* **128,** 3459–3480.

Drosdowsky, W., 1996: Variability of the Australian summer monsoon at Darwin: 1957–1992. *J. Climate,* **9,** 85–96.

Hong, Y., C. D. Kummerov, and W. S. Olson, 1999: Separation of convective and stratiform precipitation using microwave brightness temperature. *J. Appl. Meteor.,* **38,** 1195–1213.

Houghton, H. G., 1968: On precipitation mechanisms and their artificial modification. *J. Appl. Meteor.,* **7,** 851–859.

Houze, R. A., Jr., 1997: Stratiform precipitation in regions of convection: A meteorological paradox? *Bull. Amer. Meteor. Soc.,* **78,** 2179–2196.

——, 2004: Mesoscale convective systems. *Rev. Geophys.,* **42,** RG4003, doi:10.1029/2004RG000150.

Hu, Z., and R. C. Srivastava, 1995: Evolution of raindrop size distribution by coalescence, breakup, and evaporation: Theory and observations. *J. Atmos. Sci.,* **52,** 1761–1783.

Hubbert, J., and V. N. Bringi, 1995: An iterative filtering technique for the analysis of copolar differential phase and dual-frequency radar measurements. *J. Atmos. Oceanic Technol.,* **12,** 643–648.

Jakob, C., 2010: Accelerating progress in global atmospheric model development through improved parameterizations: Challenges, opportunities, and strategies. *Bull. Amer. Meteor. Soc.,* **91,** 869–875.

——, and G. Tselioudis, 2003: Objective identification of cloud regimes in the tropical western Pacific. *Geophys. Res. Lett.,* **30,** 2082, doi:10.1029/2003GL018367.

Keenan, T. D., and R. E. Carbone, 1992: A preliminary morphology of precipitation systems in tropical northern Australia. *Quart. J. Roy. Meteor. Soc.,* **118,** 283–326, doi:10.1002/qj.49711850406.

——, K. Glasson, F. Cummings, T. S. Bird, J. Keeler, and J. Lutz, 1998: The BMRC/NCAR C-Band Polarimetric (C-POL) radar system. *J. Atmos. Oceanic Technol.,* **15,** 871–886.

Kumar, V. V., A. Protat, P. T. May, C. Jacob, G. Penide, S. Kumar, and L. Davies, 2013: On the effects of large-scale environment and surface conditions on convective cloud characteristics over Darwin, Australia. *Mon. Wea. Rev.,* **141,** 1358–1374.

Kumjian, M., and A. Ryzhkov, 2010: The impact of evaporation on polarimetric characteristics of rain: Theoretical model and practical implications. *J. Appl. Meteor. Climatol.,* **49,** 1247–1267.

——, and ——, 2012: The impact of size sorting on the polarimetric radar variables. *J. Atmos. Sci.,* **69,** 2042–2060.

Kummerow, C., W. Barnes, T. Kozu, J. Shiue, and J. Simpson, 1998: The Tropical Rainfall Measuring Mission (TRMM) sensor package. *J. Atmos. Oceanic Technol.,* **15,** 809–816.

Li, X., and R. C. Srivastava, 2001: An analytical solution for raindrop evaporation and its application to radar rainfall measurements. *J. Appl. Meteor.,* **40,** 1607–1616.

Ludlam, F. H., 1950: The composition of coagulation-elements in cumulonimbus. *Quart. J. Roy. Meteor. Soc.,* **76,** 52–58, doi:10.1002/qj.49707632706.

Madden, R. A., and P. R. Julian, 1972: Description of global-scale circulation cells in the tropics with a 40–50 day period. *J. Atmos. Sci.,* **29,** 1109–1123.

May, P. T., and A. Ballinger, 2007: The statistical characteristics of convective cells in a monsoon regime (Darwin, northern Australia). *Mon. Wea. Rev.,* **135,** 82–92.

——, V. N. Bringi, and M. Thurai, 2011: Do we observe aerosol Impacts on DSDs in strongly forced tropical thunderstorms? *J. Atmos. Sci.,* **68,** 1902–1910.

McFarquhar, G. M., M. Timlin, R. M. Rauber, B. J. Jewett, J. A. Grim, and D. P. Jorgensen, 2007: Vertical variability of cloud hydrometeors in the stratiform region of mesoscale convective systems and bow echoes. *Mon. Wea. Rev.,* **135,** 3405–3428.

Munchak, S. J., C. D. Kummerow, and G. Elsaesser, 2012: Relationships between the raindrop size distribution and properties of the environment and clouds inferred from TRMM. *J. Climate,* **25,** 2963–2977.

Musil, D. J., 1970: Computer modeling of hailstone growth in feeder clouds. *J. Atmos. Sci.,* **27,** 474–482.

Penide, G., V. Giraud, D. Bouniol, P. Dubuisson, C. Duroure, A. Protat, and S. Cautenet, 2010: Numerical simulation of the 7 to 9 September 2006 AMMA mesoscale convective system: Evaluation of the dynamics and cloud microphysics using synthetic observations. *Quart. J. Roy. Meteor. Soc.,* **136,** 305–323.

Pope, M., C. Jakob, and M. J. Reeder, 2009: Regimes of the north Australian wet season. *J. Climate,* **22,** 6699–6715.

Protat, A., J. Delanoë, A. Plana-Fattori, P. T. May, and E. O'Connor, 2010: The statistical properties of tropical ice clouds generated by the West-African and Australian monsoons from ground-based radar–lidar observations. *Quart. J. Roy. Meteor. Soc.,* **136,** 345–363.

——, ——, P. T. May, J. Haynes, C. Jakob, E. J. O'Connor, M. Pope, and M. C. Wheeler, 2011: The variability of tropical ice cloud properties as a function of the large-scale context from ground-based radar–lidar observations over Darwin, Australia. *Atmos. Chem. Phys.,* **11,** 8363–8384.

Rossow, W. B., and R. A. Schiffer, 1991: ISCCP cloud data products. *Bull. Amer. Meteor. Soc.,* **71,** 2–20.

Steiner, M., R. A. Houze Jr., and S. E. Yuter, 1995: Climatological characterization of three-dimensional storm structure from radar and rain gauge data. *J. Appl. Meteor.,* **34,** 1978–2007.

Stephens, G. L., and Coauthors, 2010: Dreary state of precipitation in global models. *J. Geophys. Res.,* **115,** D24211, doi:10.1029/2010JD014532.

Sun, Y., S. Solomon, A. Dai, and R. W. Portmann, 2006: How often does it rain? *J. Climate,* **19,** 916–934.

Tan, J., J. W. F. Goddard, and M. Thurai, 1995: Applications of differential propagation phase in polarization-diversity radars at S-band and C-band. *Proc. Int. Conf. on Antennas and Propagation,* Eindhoven, Netherlands, IEEE, 336–341.

Testud, J., E. Le Bouar, E. Obligis, and M. Ali-Mehenni, 2000: The rain profiling algorithm applied to polarimetric weather radar. *J. Atmos. Oceanic Technol.,* **17,** 322–356.

——, S. Oury, P. Amayenc, and R. A. Black, 2001: The concept of ''normalized'' distributions to describe raindrop spectra: A tool for cloud physics and cloud remote sensing. *J. Appl. Meteor.,* **40,** 1118–1140.

Thurai, M., V. N. Bringi, and P. T. May, 2010: CPOL radar-derived drop size distribution statistics of stratiform and convective rain for two regimes in Darwin, Australia. *J. Atmos. Oceanic Technol.,* **27,** 932–942.

Tokay, A., and D. A. Short, 1996: Evidence from tropical raindrop spectra of the origin of rain from stratiform versus convective clouds. *J. Appl. Meteor.,* **35,** 355–371.

Ulbrich, C. W., and D. Atlas, 2007: Microphysics of raindrop size spectra: Tropical continental and maritime storms. *J. Appl. Meteor. Climatol.,* **46,** 1777–1791.

Wheeler, M. C., and H. H. Hendon, 2004: An all-season real-time multivariate MJO index: Development of an index for monitoring and prediction. *Mon. Wea. Rev.,* **132,** 1917–1932.

Williams, C. R., W. L. Ecklund, and K. S. Gage, 1995: Classification of precipitating clouds in the Tropics using 915-MHz wind profilers. *J. Atmos. Oceanic Technol.,* **12,** 996–1012.

Yuter, S. E., and R. A. Houze Jr., 1995: Three-dimensional kinematic and microphysical evolution of Florida cumulonimbus. Part II: Frequency distributions of vertical velocity, reflectivity, and differential reflectivity. *Mon. Wea. Rev.,* **123,** 1941–1963.